metals

Article

Microstructure and Wear Properties of Electron Beam Melted Ti-6Al-4V Parts: A Comparison Study against As-Cast Form

Wei Quan Toh [1], Pan Wang [2], Xipeng Tan [1,*], Mui Ling Sharon Nai [2], Erjia Liu [1,*] and Shu Beng Tor [1]

1 Singapore Centre for 3D Printing, School of Mechanical and Aerospace Engineering, Nanyang Technological University, 50 Nanyang Avenue, Singapore 639798, Singapore; tohw0023@e.ntu.edu.sg (W.Q.T.); msbtor@ntu.edu.sg (S.B.T.)

2 Singapore Institute of Manufacturing Technology, 73 Nanyang Drive, Singapore 637662, Singapore; wangp@simtech.a-star.edu.sg (P.W.); mlnai@simtech.a-star.edu.sg (M.L.S.N.)

* Correspondence: xptan1985@gmail.com (X.T.); mejliu@ntu.edu.sg (E.L.); Tel.: +65-6790-5504 (X.T. & E.L.)

Academic Editor: Manoj Gupta
Received: 29 October 2016; Accepted: 15 November 2016; Published: 18 November 2016

Abstract: Ti-6Al-4V (Ti64) parts of varying thicknesses were additively manufactured (AM) by the powder-bed-based electron beam melting (EBM) technique. Microstructure and wear properties of these EBM-built Ti-6Al-4V parts have been investigated in comparison with conventionally cast Ti64 samples. Sliding wear tests were conducted using a ball-on-disc micro-tribometer under ambient conditions. Experimental results reveal that EBM-built Ti64 samples exhibited higher microhardness and an overall larger coefficient of friction as compared to the as-cast counterpart. Of interest is that the corresponding specific wear volumes were lower for EBM-built Ti64 samples, while the as-cast Ti64 showed the poorest wear resistance despite its lower coefficient of friction. Wear mechanisms were provided in terms of quantitative microstructural characterization and detailed analysis on coefficient of friction (COF) curves.

Keywords: additive manufacturing; 3D printing; electron beam melting; titanium alloys; microstructure; wear properties

1. Introduction

Metal additive manufacturing (AM), popularly known as metal three-dimensional (3D) printing, is changing the way how metals or alloys are manufactured. Powder-bed fusion is the latest developed metal AM technology, which opens up new opportunities to create complex metallic components with relatively high resolution and good dimensional accuracy control [1–3]. Ti-6Al-4V (Ti64) is the most commonly investigated metallic material in AM because of its high specific strength, excellent corrosion resistance, and good biocompatibility, which are highly demanded in aerospace and biomedical industries [4,5]. Electron beam melting (EBM®) is a representative powder-bed fusion metal AM technique that is being increasingly employed to process Ti64. It utilizes an electron beam to selectively melt a metallic powder bed given an input of a computer-aided design (CAD) model [6]. The distinct advantages associated with EBM are its ability to fabricate metallic parts more rapidly and with greater energy-efficiency as compared to its comparative technique of selective laser melting (SLM). Moreover, EBM-built parts were shown to have less residual stress than their counterparts fabricated by laser-based systems [6–9]. Hence, post-heat treatment may not be required for EBM-built metal parts, giving an added advantage that leads to greater saving of resources.

Many studies have reported on the processing, microstructure, and mechanical properties of powder-bed fusion AM Ti64 parts [5–7,9–13]. It has been found that some of the mechanical properties, particularly for tensile properties of metal AM Ti64, are comparable to those of wrought material and much better than its as-cast form [12,13]. However, there are still very limited studies involved in their wear properties that are critical for some specific applications under wear and friction conditions [14]. As known, Ti64 possesses poor wear resistance under dry sliding due to low protection exerted by tribo-oxides formed at the surface [15,16]. Therefore, it is imperative to study on wear behavior of AM Ti64 parts and know their wear properties in comparison with the counterparts manufactured via conventional methods. In our previous works published elsewhere [5,6,17–21], the microstructure and mechanical properties of the EBM-built Ti64 parts have been systematically studied. The present work aims at investigating the wear properties of EBM-built Ti64 parts with various thicknesses and making a comparative study against commercially as-cast Ti64 sample. It is supposed to be an important supplementary study to achieve better understanding for practical applications of EBM-manufactured Ti64 parts.

2. Experimental Section

2.1. Materials, Fabrication, and Sample Preparation

All the EBM-built samples were fabricated via an Arcam A2XX (Arcam AB, Mölndal, Sweden) EBM machine, which has a build chamber of Φ420 mm × 380 mm. A schematic diagram of a typical EBM machine is illustrated in Figure 1. The powder used in this process was Ti-6Al-4V ELI (Grade 23) (Batch No. 877) supplied by Arcam AB, and was mainly spherical in shape, as shown in Figure 2a. The spherical nature of the powder assures good followability and thus consistency in the spreading of powder during raking. The powder had a size distribution ranging from 45 to 105 μm, while the mean particle size was 61.8 μm ± 23.8 μm. A summary on the powder size distribution of Ti64 used during fabrication is as depicted in Figure 2b. The nominal composition of the Ti64 powder is as follows: 6.0Al-4.0V-0.03C-0.1Fe-0.1O-0.01N-<0.003H and the balance being Ti (wt. %). The EBM-built samples of varying thicknesses of 0.5 mm, 1 mm, 5 mm, 10 mm, and 20 mm by 100 mm in length and 30 mm in height are shown in Figure 3a. They were termed 0.5 mm, 1 mm, 5 mm, 10 mm, and 20 mm samples, respectively. The build chamber was under a controlled vacuum environment having a temperature range of 600 to 650 °C. The samples were built on a 210 mm × 210 mm stainless steel (SS) start plate. The samples were subsequently removed from the SS start plate via knocking on the backside of the SS plate and cleaned with the use of the powder recovering system (PRS). PRS primarily functioned as a grit blaster where blasting media (Ti64) were accelerated towards the sample surface with the aid of high velocity compressed air with the aim to remove any residual partially-sintered and unmelted powder particles surrounding the samples' surface. The as-cast samples were supplied in the form of a rod by Titan Engineering Pte. Ltd. (Singapore, Singapore), cast to the specification ASEM B348 GR5 and had a dimension of Φ25.4 mm × 1500 mm. The EBM-built samples were sliced from the middle section (X–Z plane) into squares of 20 mm × 20 mm, while the as-cast sample was sliced into a disc of Φ25.4 mm × 5 mm. All the samples were then hot mounted with phenolic polymer and subsequently polished to a mirror-like finish.

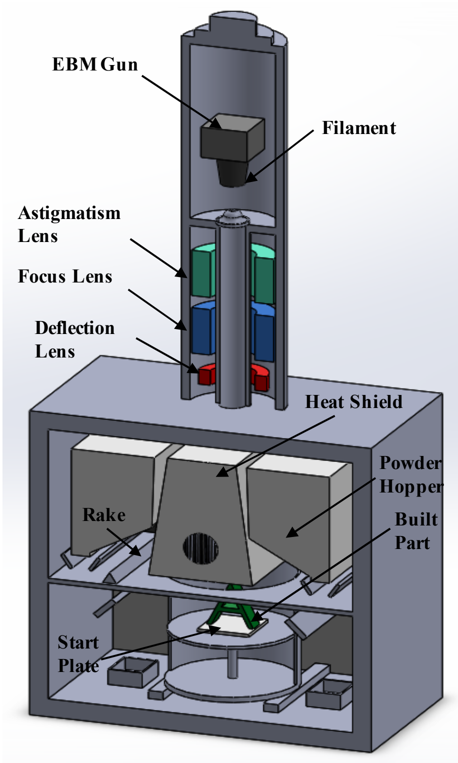

Figure 1. Schematic of an Arcam A2XX EBM machine.

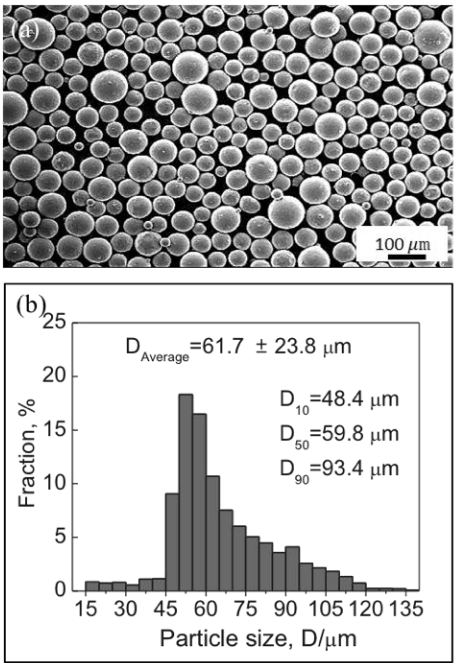

Figure 2. (**a**) SEM image and (**b**) powder size distribution of Ti64 powder supplied by Arcam AB.

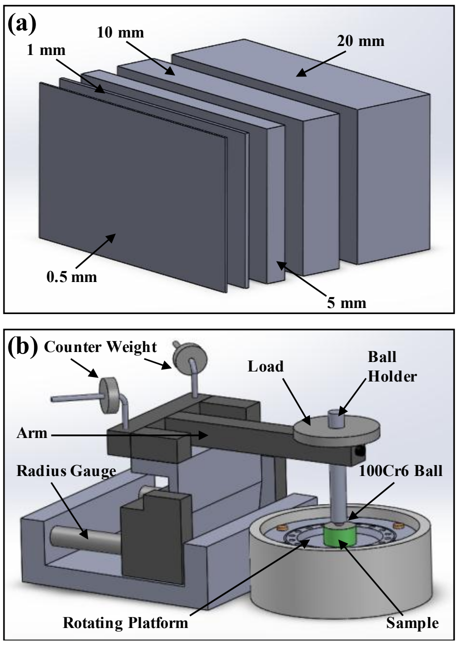

Figure 3. (**a**) Schematic of EBM-built Ti64 samples with thicknesses of 0.5, 1, 5, 10, and 20 mm; (**b**) Schematic configuration of the ball-on-disc micro-tribometer.

2.2. Powder Analysis

Morphological characteristics of the Ti64 powder were determined using a Malvern Morphologi G3 S (Malvern Instruments Ltd., Worcestershire, UK). Powder samples of 5 mm^3 in volume were dispersed on the glass plate. A 5× objective was used for the measurement of this study. Four parameters of particle size viz. D_{10}, D_{50}, D_{90}, and D_{average} (size below which 10%, 50%, 90%, and average particle size are present, respectively) were calculated from the particle size distribution curve.

2.3. Surface Analysis

Surface roughness of as-built and as-polished Ti64 samples, and worn surfaces were examined using a surface profilometer (Talyscan 150) (Taylor Hobson Inc., Rolling Meadows, IL, USA) with a diamond stylus of 4 μm in diameter. Chemical compositions of as-built and as-polished surfaces were analyzed with the aid of X-ray photoelectron spectroscopy (XPS; Kratos AXIS Ultra, Kratos Analytical Ltd., Manchester, UK). Both the as-built and the as-polished samples were sliced from the other side of the squares and cut into pieces of 10 mm × 10 mm × 2 mm. All of the Ti64 samples were ultrasonically cleaned in acetone and ethanol for 30 min respectively and stored in dry box overnight before analysis was carried out.

2.4. Microstructural Characterisation Techniques

Microstructure, wear morphology and wear debris were examined using a scanning electron microscope (SEM; JEOL-JSM-5600LV; 20 kV, JEOL Ltd., Akishima, Japan). Chemical composition of the wear debris was examined by energy-dispersive X-ray spectroscopy (EDX) (Oxford Instruments Plc., Abingdon, UK) equipped within the SEM. In addition, X-ray diffraction (XRD; PANalytical Empyrean; Cu Kα; 40 mA; 40 mV; step size of 0.01°) (PANalytical, Almelo, The Netherlands) was employed for phase identification.

2.5. Mechanical Properties Evaluation

Vickers microhardness tests were carried out on the slightly-etched samples using a Vickers micro-indentor (Future-tech FM-300e) (FUTURE-TECH Corp., Fujisaki, Japan) with an applied load of 1 kg and a dwell time of 15 s. Sliding wear tests were carried out on polished surfaces, using a ball-on-disc micro-tribometer (CSM model, Anton Paar Gmbh, Graz, Austria) as shown in Figure 3b at room temperature of 23 °C and in the ambient environment. A 100Cr6 steel ball of Φ6 mm was used as counter-face with an applied load of 1 N on the rotating Ti64 samples in a circular path of 3 mm in diameter at a linear sliding velocity of 2 cm/s for 50,000 laps. For all of the EBM-built samples, the X–Z plane was wear tested. Based on the measured wear width and wear depth, wear volume was calculated via a simple geometrical equation. Specific wear rates [22] were then evaluated by normalizing the wear volume with the load applied (N) and sliding distance (m).

3. Results and Discussion

3.1. Microstructure

Figure 4 shows the microstructure of the EBM-built and as-cast Ti64 samples. It can be clearly seen that both the 0.5 mm and 1 mm samples have similar alternate α/β microstructures mixed with acicular α' martensite, which is different from the rest of the EBM-built samples and the as-cast sample, which have α/β microstructures. Of particular difference is that coarse β was observed in the as-cast sample. Additionally, the results obtained from the XRD patterns shown in Figure 5 revealed peak shifting phenomenon in the EBM-built 1 mm sample as compared to the 20 mm and the as-cast Ti64 sample. This peak shifting phenomenon is in line with the studies by Zeng et al. [23] that suggest the presence of α' martensite. The appearance of α' phase in 0.5 mm and 1 mm was also confirmed by TEM observation [5,18]. In the case of the EBM-built samples two types of typical transformed α/β structure was observed, namely, the colony and the basket-weave (also known as Widmanstätten) morphologies. As a result of the difference in microstructure, they have different microhardness values which will be given in the following sections. From the results, it is known that the acicular α' phase causes a higher hardness value as compared to the α/β microstructure seen in the rest of the EBM-built samples. In addition, the microhardness of EBM-built Ti64 samples decreases with the increase in sample thickness. This is due to the fast cooling rate coupled with the EBM build temperature, favoring the formation of α' martensite in the thin samples [10,18]. The as-cast sample has the lowest hardness value due to its coarse α/β microstructure, which is largely caused by the moderate cooling rate during the casting process [14,24].

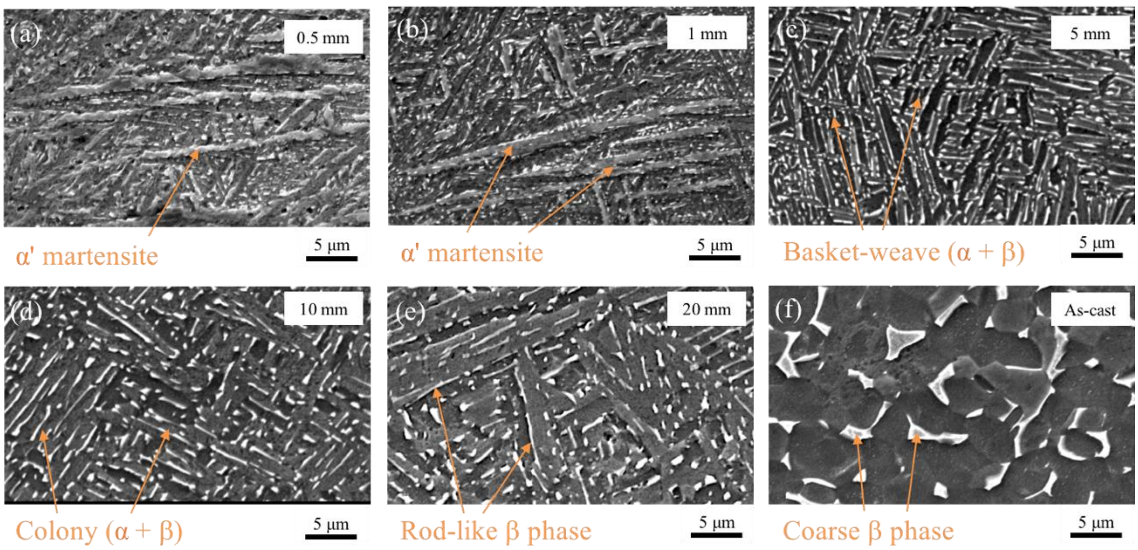

Figure 4. (**a**–**f**) SEM micrographs of EBM-built Ti64 samples with thicknesses of 0.5, 1, 5, 10, and 20 mm and the as-cast Ti64 samples, respectively. Microstructural features are indicated by arrows.

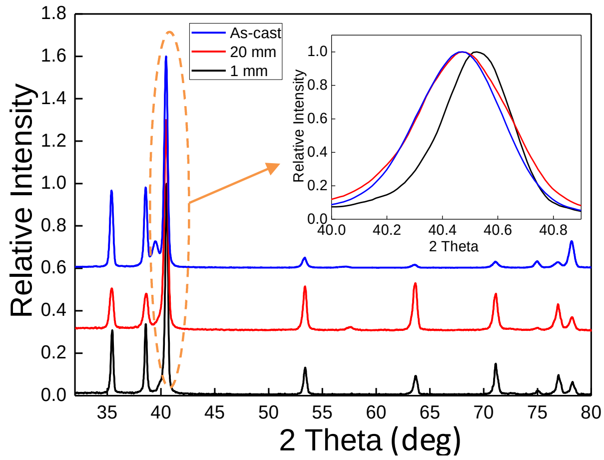

Figure 5. XRD patterns for 1 mm and 20 mm EBM-built and as-cast Ti64 samples.

3.2. Surface Conditions

Figure 6 shows 3D surface mappings of the EBM as-built 20 mm sample and the as-polished 20 mm sample for dry sliding wear tests. To our authors' best knowledge, the rough build surface of AM-fabricated parts may be the main obstacle to their direct practical applications. From Figure 6, it can be obtained that EBM as-built Ti64 samples have an average surface roughness of 34.4 µm. In order to avoid the influence of rough surfaces on wear properties, all of the samples were polished to a mirror-like finish with roughness of ~0.3 µm. XPS survey spectra for both the EBM-built 20 mm Ti64 sample and Ti64 powder used for EBM fabrication are shown in Figure 7. In both XPS spectra, it was dominated by strong signals of titanium (Ti), carbon (C), and oxygen (O). Of particular interest is that the signal for aluminum (Al) was detected on the Ti64 powder surface. But not on the sample surface. This may suggest that the surface oxide form on the EBM samples were predominately Ti and O. The presence of carbon on both instances were not unusual based on previous literatures [25] and the detection of carbon is mainly a result of adsorption of organic molecules from the environment. A detailed scan of the elements present on the surface of the Ti64 samples were carried out and illustrated in Figure 8a,b, where the Ti 2p and O 1s peak of the EBM-built 20 mm sample were revealed, respectively. The Ti 2p peak has symmetrical peak shapes, which is in line with the formation of titanium dioxide (TiO_2). Correspondingly, the asymmetrical shape of the O 1s peak put forward that oxide was formed with more than one metal element. Following the decomposition of the O 1s peak in Figure 8b revealed that both TiO_2 and Al_2O_3 were formed. However, since Al is not detectable via XPS on the EBM-built surface, it is strongly suggested that the surfaces of all the EBM-built samples are mainly comprised of TiO_2. The instantaneous formation of a surficial TiO_2 layer is supposed to be the influential factor inducing poor wear resistance of Ti64.

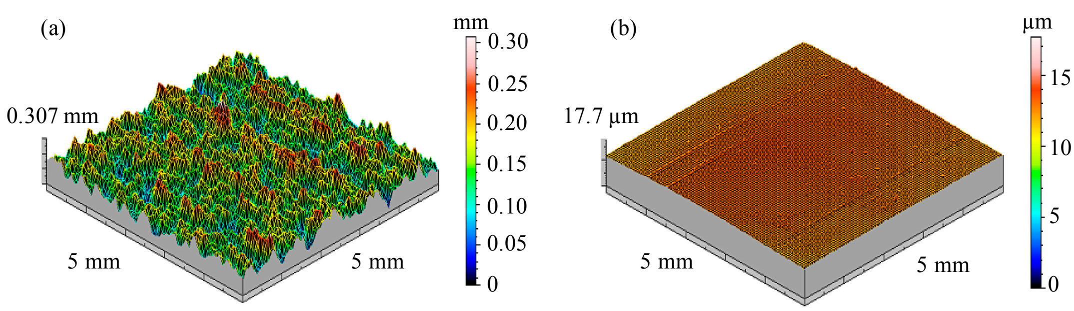

Figure 6. Representative surface profiles of the EBM Ti64 20 mm samples of (**a**) as-built and (**b**) as-polished.

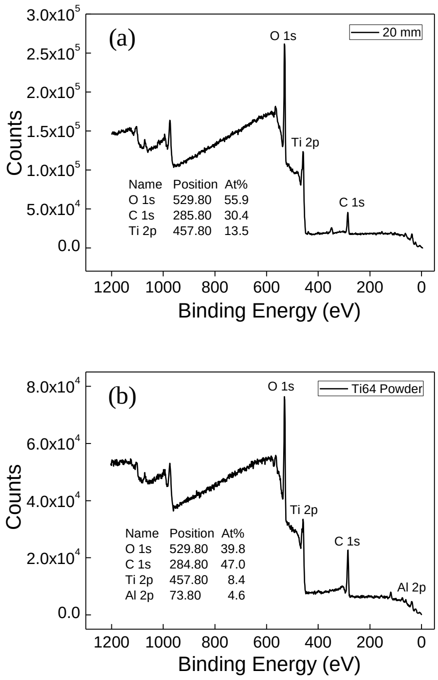

Figure 7. XPS survey spectra for (**a**) the 20 mm EBM-built Ti64 sample and (**b**) the Ti64 powder.

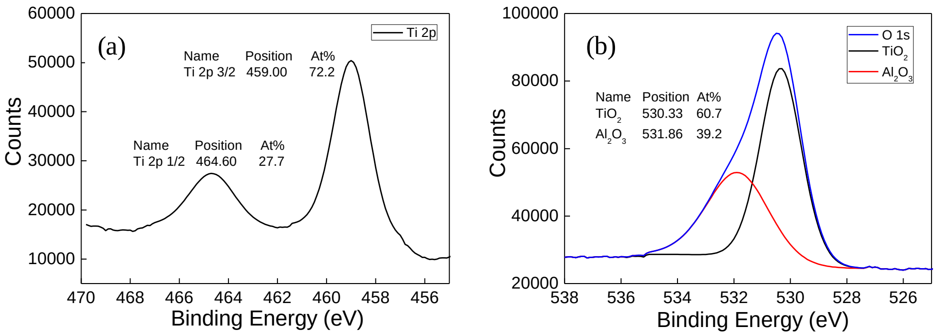

Figure 8. XPS spectra of the (**a**) Ti 2p peak and (**b**) O 1s peak on the surface of the 20 mm EBM-built Ti64 sample.

3.3. Dry Sliding Wear Behaviour

The representative coefficient of friction (COF) curves are displayed in Figure 9a. Similar wear characteristics were observed, regardless of the different microstructures existed inside the EBM-built and the as-cast samples. In the insert shown in Figure 9a, it is noted that the wear characteristics of the Ti64 sample can be classified into four major stages:

(I) Wearing-in period, where the friction coefficient increases rapidly when the ball is in direct contact with the oxide layer of sample surface.
(II) Cushioning of the oxide layer, which is characterized by a slight decrease in COF, probably due to surface oxide that prevents direct metal-metal contact between the ball and the Ti64 sample.
(III) Breakage of the oxide layer into fragments, which was indicated by a significant increase in COF. In this stage, the oxide debris generated were fragmented as a result of repeated cycles of stress and load during sliding. This, coupled with the complete removal of the oxide layer, allows the direct metal-metal contact and, as such, causes the increase in COF.
(IV) Stabilization of COF, which occurs after ~10,000 laps.

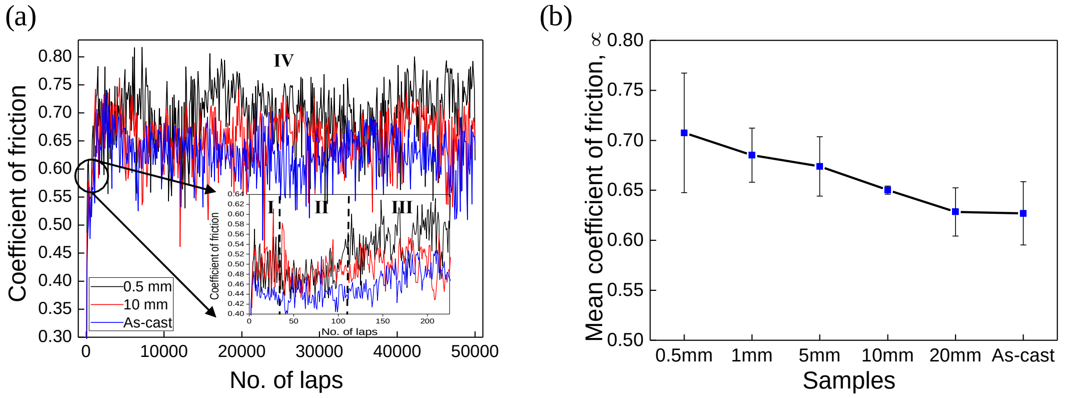

Figure 9. (**a**) COF curves of Ti64 samples as a function of number of sliding laps. (**b**) Mean COFs of EBM-built and as-cast Ti64 samples.

Figure 9b shows the mean COF values calculated from three groups of experimental data. It is revealed that the thin 1 mm sample has a higher COF than the 10 mm sample, and the lowest being the as-cast sample. The larger deviation of COF values in 0.5 mm sample is mainly attributed to the obvious martensite protrusions within its microstructure. Moreover, we observed that the mean COF of the 20 mm sample was nearly the same as the as-cast sample, while COFs of the rest of the EBM-built samples increased with the decrease in sample thickness. Interestingly, the thinnest EBM-built sample with the highest mean COF has the lowest specific wear rate (as seen in Figure 10a). Moreover, the specific wear rate increased with increase in sample thickness. Figure 10b reveals the 2-D depth profiles of the samples' wear tracks correspondingly. The decrease in specific wear rate with decrease in sample thickness is mainly due to the increased hardness as a result of the finer microstructure and the presence of α' in the thinner EBM-built samples. In general, an increase in hardness will correspondingly lead to an increase in shear strength of the material, and it possibly results in a higher friction coefficient [22]. A higher shear strength defines a higher ability to resist plastic shearing during sliding and as such a higher wear resistance [22]. Therefore, it may suggest that the thinner EBM-built sample, which has a higher hardness because of the fast cooling rate as compared to the as-cast sample, exhibits high wear resistance and, as such, reduces the roughening of the surface during rubbing and, thus, produces lesser wear debris. This, consequently, results in a lower specific wear rate but a high mean COF.

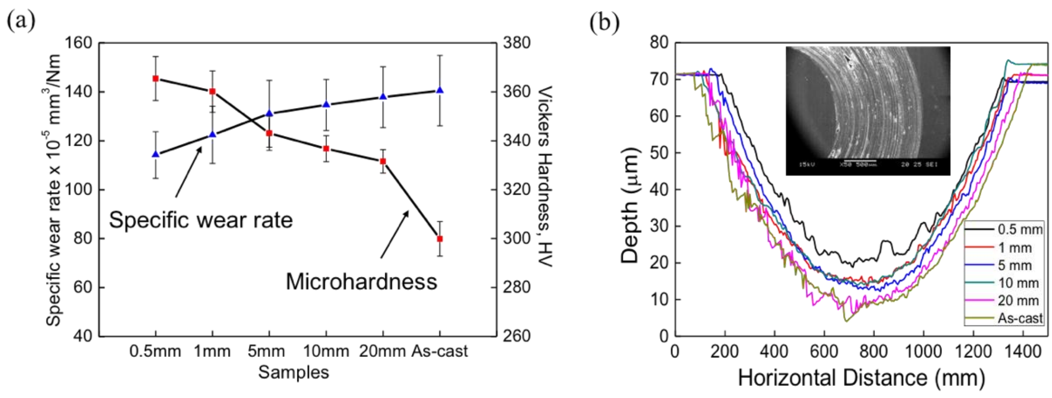

Figure 10. (**a**) Specific wear rates and microhardness values of EBM-built and as-cast Ti64 samples; (**b**) Surface profiles measured across the wear tracks of the worn Ti64 samples.

The global wear rate (W_{global}) of a Ti64 sample can be depicted by the combination of oxidative wear ($W_{oxidative}$) and delamination wear ($W_{delamination}$) and is given by [16,26,27]:

$$W_{global} = W_{oxidative} + W_{delamination} = \frac{A_r C^2 A}{v z_c \exp\left(-\frac{Q}{RT_f}\right)} + k\frac{F_N}{H} \quad (1)$$

where A_r is the real area of contact, C is the material constant, A is the Arrhenius constant for oxidation, v is the sliding speed, z_c is the critical thickness of oxide film, Q is the activation energy for oxidation, R is the molar gas constant, T_f is the flash temperature, k is the wear coefficient, F_N is the normal load, and H is the hardness. Figure 11a,b reveal the SEM images of the wear debris and the wear track of the 0.5 mm sample respectively. The indication of the transfer layers and oxide particles in Figure 11a and the surface cracks that are perpendicular to the sliding direction in Figure 11b give a valuable insight into the wear mechanism of Ti64, which is consistent with the global wear rate proposed by Al Molinari et al. [16]. Nevertheless, a simple calculation of the theoretical delamination wear rate using the sample's respective average hardness value obtained from the earlier Vickers hardness measurement as shown in Table 1, even without consideration of oxidative wear, revealed a higher wear rate as compared to the experimental obtained global wear rate value by two factors. This may be owning to the formation of a tribo-layer that avoids the direct metal-metal contact between the asperities of the steel ball and the asperities of the Ti64 sample, thereby preventing further wear through sliding.

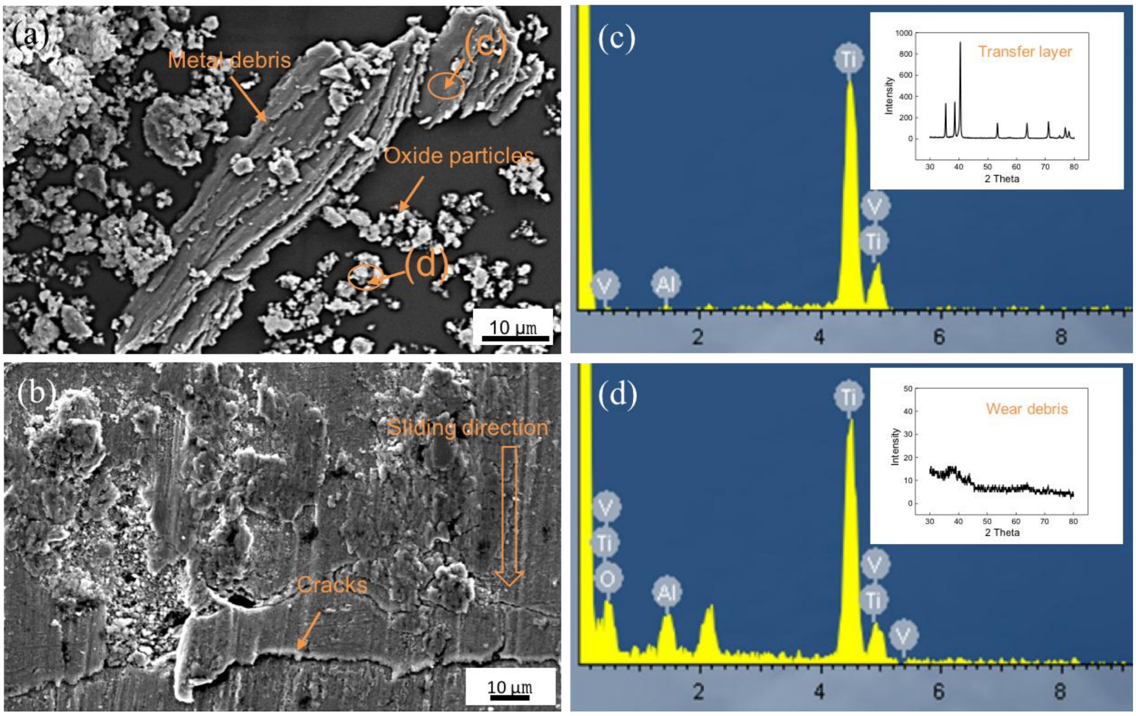

Figure 11. (**a**) SEM micrograph of the transfer layers generated by sliding on the 0.5 mm EBM-built sample; (**b**) SEM micrograph of the wear track on the 0.5 mm EBM-built sample after wear test; (**c**) EDX spectrum and inserted XRD patterns of the transfer layers and (**d**) EDX spectrum and inserted XRD patterns of the oxide particles that were generated during sliding on the 0.5 mm EBM-built sample. The detection locations of (**c**) and (**d**) were indicated in (**a**).

Table 1. Comparison between the calculated theoretical delamination wear rate (W_d) and the actual global wear rate ($W_{G(exp)}$).

Samples	W_d ($\times 10^{-12}$ m^3/m)	$W_{G(exp)}$ ($\times 10^{-12}$ m^3/m)
0.5 mm	198.3	1.1
1 mm	195.6	1.2
5 mm	200.9	1.3
10 mm	195.3	1.3
20 mm	194.4	1.3
As-cast	208.7	1.4

The tribo-layer is commonly formed on a metal surface when rubbed by a counterface during a sliding wear test [28]. In order to further explore the wear characteristics and mechanisms of the EBM-built and as-cast Ti64, it is first necessary to delineate the terms of the non-oxide tribo-layer and tribo-oxide layer. In the case of non-oxide tribo-layer, it merely refers to the oxides that could not be identified by XRD and are not completely absent of an oxide on the Ti64 sample surface. On the other hand, the tribo-oxide layer refers to the formation of a strong and compact oxide layer during sliding process that serves as a protection to the worn surface [28–30]. Inherently, in an EBM process where the built condition is under high vacuum environment, the thickness of surface oxide layer only ranges from 5 to 7 nm [31]. Moreover, all the wear tests were conducted at room temperature. As a result, the formed oxide layer was weak and incompact, thus allowing the ease of delamination of the oxide layer. In our experiment, white fragmented particles were observed from both the SEM images of the 0.5 mm sample in Figure 11a, where the white particles indicate the breakdown of the oxide layer into oxide particles. This observation can be reinforced from the EDX spectra in Figure 11c,d. Moreover, due to the harsh nature during sliding, the wear debris formed was black and powdery in nature. Subsequent XRD analysis of the wear debris suggests that the oxide particles were mainly amorphous in nature. On the contrary, EDX was unable to detect the presence of oxygen on the transfer layer (see Figure 11c) that was removed from the bulk sample lying beneath the oxide surface.

Making reference to all the results obtained in the analysis, a wear mechanism was proposed and exemplified in Figure 12. Because of the reactive nature of titanium, TiO_2 was subsequently formed as an oxide layer on the sample surface, which has been proven by the XPS results in Figure 8. During dry sliding, the TiO_2 layer which serves as a protection layer of the substrate surface was first removed, thus generating flakes of oxide debris. Consequently, under loading and repeated rubbing, coupled with the brittle nature of the oxide debris, some of these debris were further broken up into fragmented oxide particles. Further sliding results in the compete removal of the oxide layer, thereby allowing the direct metal-metal contact between the asperities of the counter ball and the sample surface. Accordingly, bulk metal material was removed, which formed the metal debris. As the removal of the bulk metal from the substrate surface is continuous and instantaneous, oxide may not be able to form readily on the metal debris surface and as such allowing these metal debris layers to adhere (transfer layer) together. However, as the sliding process in the experiment was relatively slow to the ones reported in the literature, the centrifugal force induced during sliding was not able to remove the oxide debris, particles, and transfer layer from the sample surface. Therefore, these remaining materials allow for the formation of a compact tribo-layer that subsequently prevents further removal of the metal material from the substrate surface.

In our present experiment of low speed sliding (2 cm/s), the non-oxide tribo-layer was formed as a result of both oxide particles and metal debris. Additionally, our current experiment results also reveal that the global wear rate is two orders lower compared to that from the theoretical calculation. This could be owing to the fact that the theoretical equation may not take into account the actual physical condition during sliding. With reference to the proposed wear mechanism illustrated in Figure 12, at a very low speed of 2 cm/s, it was observed that the oxide particles and metal debris still remain on the wear track surface. Hence, this tribo-layer was not pushed away through centrifugation movement during the sliding process and thus acted as a protection layer between the counter ball and Ti64 sample, thereby preventing direct metal-metal contact, leading to a lower wear rate.

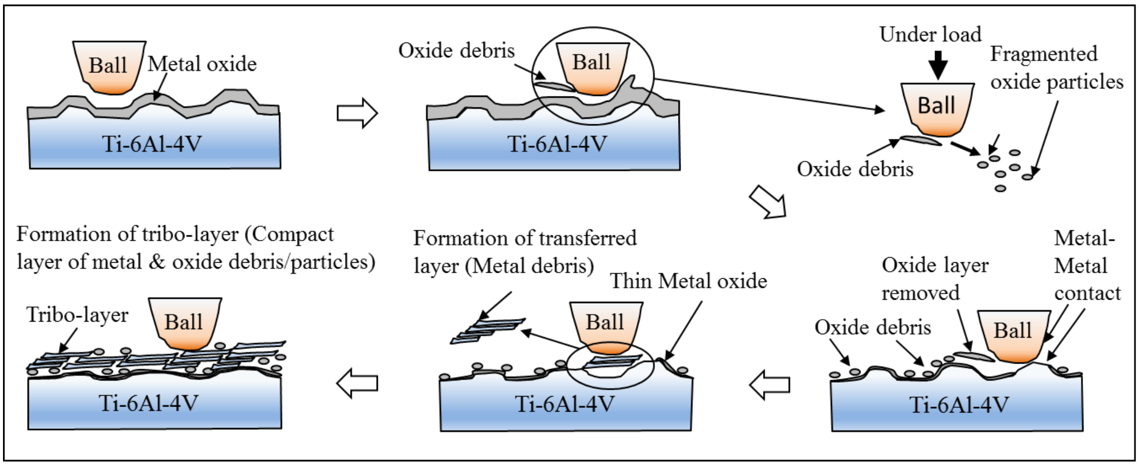

Figure 12. Schematic road-map on the formation of tribo-layer during sliding wear of Ti64 samples.

4. Summary

Due to the fast cooling rate that was inherently involved in a typical EBM process, it was observed that the thinner EBM-built Ti64 samples (0.5 mm and 1 mm thick) had much finer microstructure and higher microhardness as compared to the as-cast form. However, they showed similar wear characteristics, regardless of the different microstructures within the EBM-built and the as-cast samples. The higher hardness of the EBM-built samples resulted in their higher wear resistance and intrinsically lower wear rate. It is worth noting that all of the wear rates obtained in our experiment were lower as compared to the theoretical estimation. It could be due to the mild wear conditions (e.g., a very low sliding speed of 2 cm/s) and the formation of the tribo-layer that remained on the wear track, acting as a protection barrier between the counter ball and the Ti64 substrate. We can conclude that the EBM process is capable of manufacturing Ti64 parts with superior wear properties compared to the as-cast counterparts.

Acknowledgments: The authors are grateful for financial support provided by A*Star Industrial Additive Manufacturing Program: Work Package 3. We acknowledge the use of resources in Singapore Centre for 3D Printing (SC3DP) funded by the National Research Foundation (NRF), Singapore.

Author Contributions: W.Q.T. examined the specimens and wrote the main paper. X.T. designed the experiments and fabricated the Ti64 samples using EBM. W.Q.T., X.T., P.W. and M.L.S.N. performed specimen preparation and characterization. E.L. and S.B.T. supervised the project. All authors discussed the results and finalized the paper.

Conflicts of Interest: The authors declare no conflict of interest.

References

1. Frazier, W.E. Metal Additive Manufacturing: A Review. *J. Mater. Eng. Perform.* **2014**, *23*, 1917–1928. [CrossRef]
2. Gibson, I.; Rosen, D.W.; Stucker, B. *Additive Manufacturing Technologies*; Springer: Berlin, Germany, 2010.
3. Chua, C.K.; Leong, K.F. *3D Printing and Additive Manufacturing: Principles and Applications*; World Scientific: Singapore, 2015.
4. Boyer, R.; Welsch, G.; Collings, E.W. *Materials Properties Handbook: Titanium Alloys*; ASM International: Materials Park, OH, USA, 1994.
5. Tan, X.P.; Kok, Y.; Toh, W.Q.; Tan, Y.J.; Descoins, M.; Mangelinck, D.; Tor, S.B.; Leong, K.F.; Chua, C.K. Revealingmartensitic transformation and α/β interface evolution in electron beam melting three-dimensional-printed Ti-6Al-4V. *Sci. Rep.* **2016**, *6*, 26039. [CrossRef] [PubMed]

6. Kok, Y.; Tan, X.P.; Tor, S.B.; Chua, C.K. Fabrication and microstructural characterisation of additive manufactured Ti-6Al-4V parts by electron beam melting. *Virtual Phys. Prototyp.* **2015**, *10*, 13–21. [CrossRef]
7. Yadroitsev, I.; Yadroitsava, I. Evaluation of residual stress in stainless steel 316L and Ti6Al4V samples produced by selective laser melting. *Virtual Phys. Prototyp.* **2015**, *10*, 67–76. [CrossRef]
8. Sun, Z.J.; Tan, X.P.; Tor, S.B.; Yeong, W.Y. Selective laser melting of stainless steel 316L with low porosity and high build rates. *Mater. Des.* **2016**, *104*, 197–204. [CrossRef]
9. Do, D.K.; Li, P. The effect of laser energy input on the microstructure, physical and mechanical properties of Ti-6Al-4V alloys by selective laser melting. *Virtual Phys. Prototyp.* **2016**, *11*, 41–47. [CrossRef]
10. Al-Bermani, S.S.; Blackmore, M.L.; Zhang, W.; Todd, I. The Origin of Microstructural Diversity, Texture, and Mechanical Properties in Electron Beam Melted Ti-6Al-4V. *Metall. Mater. Trans. A* **2010**, *41*, 3422–3434. [CrossRef]
11. Rafi, H.K.; Karthik, N.V.; Gong, H.; Starr, T.L.; Stucker, B.E. Microstructure and mechanical properties of Ti6Al4V parts fabricated by selective laser melting and electron beam melting. *J. Mater. Eng. Perform.* **2013**, *22*, 3872–3883. [CrossRef]
12. Lewandowski, J.; Seifi, M. Metal additive manufacturing: A review of mechanical properties. *Annu. Rev. Mater. Res.* **2016**, *46*, 151–186. [CrossRef]
13. Qian, M.; Xu, W.; Brandt, M.; Tang, H.P. Additive manufacturing and postprocessing of Ti-6Al-4V for superior mechanical properties. *MRS Bull.* **2016**, *41*, 775–783. [CrossRef]
14. Attar, H.; Prashanth, K.G.; Chaubey, A.K.; Calin, M.; Zhang, L.C.; Scudino, S.; Eckert, J. Comparison of wear properties of commercially pure titanium prepared by selective laser melting and casting processes. *Mater. Lett.* **2015**, *142*, 38–41. [CrossRef]
15. Budinski, K.G. Tribological properties of titanium alloys. *Wear* **1991**, *151*, 203–217. [CrossRef]
16. Molinari, A.; Straffelini, G.; Tesi, B.; Bacci, T. Dry sliding wear mechanisms of the Ti6Al4V alloy. *Wear* **1997**, *208*, 105–112. [CrossRef]
17. Wang, P.; Nai, M.L.S.; Sin, W.J.; Wei, J. Effect of Building Height on Microstructure and Mechanical Properties of Big-Sized Ti-6Al-4V Plate Fabricated by Electron Beam Melting. *MATEC Web Conf.* **2015**, *30*, 02001. [CrossRef]
18. Tan, X.P.; Kok, Y.; Tan, Y.J.; Vastola, G.; Pei, Q.X.; Zhang, G.; Zhang, Y.W.; Tor, S.B.; Leong, K.F.; Chua, C.K. An experimental and simulation study on build thickness dependent microstructure for electron beam melted Ti-6Al-4V. *J. Alloy. Compd.* **2015**, *646*, 303–309. [CrossRef]
19. Tan, X.P.; Kok, Y.; Tan, Y.J.; Descoins, M.; Mangelinck, D.; Tor, S.B.; Leong, K.F.; Chua, C.K. Graded microstructure and mechanical properties of additive manufactured Ti-6Al-4V via electron beam melting. *Acta Mater.* **2015**, *97*, 1–16. [CrossRef]
20. Wang, P.; Tan, X.P.; Nai, M.L.S.; Tor, S.B.; Wei, J. Spatial and geometrical-based characterization of microstructure and microhardness for an electron beam melted Ti-6Al-4V component. *Mater. Des.* **2016**, *95*, 287–295. [CrossRef]
21. Kok, Y.; Tan, X.P.; Loh, N.H.; Tor, S.B.; Chua, C.K. Geometry dependence of microstructure and microhardness for selective electron beam melted Ti-6Al-4V parts. *Virtual Phys. Prototyp.* **2016**, *11*, 183–191. [CrossRef]
22. Hutchings, I.M. *Tribology: Friction and Wear of Engineering Materials*; Edward Arnold: London, UK, 1992.
23. Zeng, L.; Bieler, T.R. Effects of working, heat treatment, and aging on microstructural evolution and crystallographic texture of α, α', α'' and β phases in Ti-6Al-4V wire. *Mater. Sci. Eng. A.* **2005**, *392*, 403–414. [CrossRef]
24. Jovanović, M.T.; Tadić, S.; Zec, S.; Mišković, Z.; Bobić, I. The effect of annealing temperatures and cooling rates on microstructure and mechanical properties of investment cast Ti-6Al-4V alloy. *Mater. Des.* **2006**, *27*, 192–199. [CrossRef]
25. Karlsson, J.; Snis, A.; Engqvist, H.; Lausmaa, J. Characterization and comparison of materials produced by electron beam melting of two different Ti-6Al-4V powder fractions. *J. Mater. Process. Technol.* **2013**, *213*, 2109–2118. [CrossRef]
26. Lim, S.; Ashby, M. Overview No. 55 wear-mechanism maps. *Acta Metall.* **1987**, *35*, 1–24. [CrossRef]
27. Ashby, M.; Lim, S. Wear-mechanism maps. *Scr. Metall. Mater.* **1990**, *24*, 805–810. [CrossRef]
28. Zhang, Q.Y.; Zhou, Y.; Wang, L.; Cui, X.H.; Wang, S.Q. Investigation on tribo-layers and their function of a titanium alloy during dry sliding. *Tribol. Int.* **2016**, *94*, 541–549. [CrossRef]

29. Alam, M.O.; Haseeb, A. Response of Ti-6Al-4V and Ti-24Al-11Nb alloys to dry sliding wear against hardened steel. *Tribol. Int.* **2002**, *35*, 357–362. [CrossRef]
30. Dong, H.; Bloyce, A.; Morton, P.; Bell, T. Surface engineering to improve tribological performance of Ti-6Al-4V. *Surf. Eng.* **1997**, *13*, 402–406. [CrossRef]
31. Karlsson, J.; Norell, M.; Ackelid, U.; Engqvist, H.; Lausmaa, J. Surface oxidation behavior of Ti-6Al-4V manufactured by Electron Beam Melting (EBM®). *J. Manuf. Process.* **2015**, *17*, 120–126. [CrossRef]